Synchrotron X-ray diffraction study of the structure and dehydration behavior of todorokite

JEFFREY E. POST,[1,*] PETER J. HEANEY,[2] AND JONATHAN HANSON[3]

[1]Department of Mineral Sciences, Smithsonian Institution, Washington, D.C. 20560-0119, U.S.A.
[2]Department of Geosciences, 309 Deike, Pennsylvania State University, University Park, Pennsylvania 16802, U.S.A.
[3]Chemistry Department, Brookhaven National Laboratory, Upton, New York 11793, U.S.A.

ABSTRACT

Real-time, temperature-resolved synchrotron powder X-ray diffraction data and Rietveld refinements were used to investigate the behavior of the todorokite structure from 100 to 820 K. At 298 K, the lower valence cations, such as Mn^{3+}, occupy large octahedral sites at the edges of the triple chains, and four water/cation sites are in the tunnels. In our heating experiments in vacuum, todorokite began to break down at ~450 K and fully decomposed by 620 K, at which point hausmannite started to form. Our results suggest that the loss of O_2 accompanied the reduction of Mn^{4+} to Mn^{3+} and Mn^{2+}, and these reactions impelled a breakdown of the octahedral framework and the subsequent release of the tunnel water molecules. Rietveld refinements revealed a gradual thermal expansion of the todorokite structure to ~450 K. At higher temperatures, the unit-cell volume gradually decreased, primarily as a result of a decrease in c, and the decline in β with increasing temperature was accelerated. A mechanism for forming the inverse spinel hausmannite structure from todorokite is presented.

INTRODUCTION

Microporous and layer manganese oxide minerals act as important chemical controls in soils and sediments and associated water systems, and with their synthetic analogs they are valued for their catalytic, ion exchange, electrochemical, and adsorption properties (Weisz 1968; Nitta 1984; Shen et al. 1993; Kanoh et al. 1997; Dyer et al. 2000). The atomic frameworks of these materials are constructed from Mn-O octahedra that share edges and link corners to yield a panoply of phases with tunnel or layer structures. Of particular interest have been Mn-oxide catalysts with large tunnel structures, which are also known as octahedral molecular sieves (OMS). Because these materials exhibit a range of tunnel shapes and sizes, they offer selectivity for particular species in chemical reactions and the potential for a range of complementary catalytic or cation-exchange applications.

Some of the most promising and intensely studied Mn-oxide catalysts are those with the todorokite structure because of their large tunnels and ease of preparation. Todorokite occurs in a wide variety of geological settings, including oxidized zones of Mn-rich deposits, as coatings on stream boulders, and in soils and sediments. It is also the major Mn-oxide phase in ocean Mn nodules and recently was recognized as an important component in rock varnishes (McKeown and Post 2001). Scientists have developed a variety of methods for synthesizing todorokite-like materials (Golden et al. 1986; Shen et al. 1993; Luo et al. 1999; Nicolas-Tolentino et al. 1999; Vileno et al. 1999), and these synthetic todorokites have been shown to be effective cathode materials for rechargeable Li batteries

(Duncan et al. 1998), selective ion-exchange agents for immobilization of certain metal radionuclides (Dyer et al. 2000), and oxidative catalysts (Shen et al. 1993; Brock et al. 1998; Vileno et al. 1999).

Until recently (Post et al. 1999), todorokite held the record for the largest tunnels of any natural or synthetic Mn-oxide phase. In todorokite, triple chains of edge-sharing $Mn^{4+,3+}$-O octahedra share corners to form tunnels with square cross sections that measure three octahedra per side (3×3) (Post and Bish 1988) (Fig. 1). The tunnels in natural samples are partially filled with water molecules and a variety of cations, including Mg^{2+}, Ca^{2+}, K^+, Na^+, and Ba^{2+}. Because natural and synthetic todorokite samples typically are fine-grained and poorly crystalline, it has not been possible to study the crystal structure using single-crystal diffraction methods, and consequently many details of the structure are still not well known. A Rietveld refinement by Post and Bish (1988) provided the first comprehensive structure for todorokite, including positions of some of the tunnel species. Their study was limited, however, because it relied upon powder X-ray diffraction data collected using a conventional sealed-tube source, and refinements were performed with less sophisticated Rietveld codes than are available today. Consequently, some of the resulting Mn-O bond distances were unrealistically short (e.g., 1.75 and 1.82 Å) and only a portion of the tunnel sites were identified.

A more complete understanding of the todorokite structure and its thermal behavior is relevant to many of its proposed uses and to understanding its role in geochemical systems. In the present study, we report the most precise and in-depth description of the todorokite structure to date as derived from Rietveld refinements using synchroton powder X-ray diffraction data collected at room temperature and at 100 K. The high-
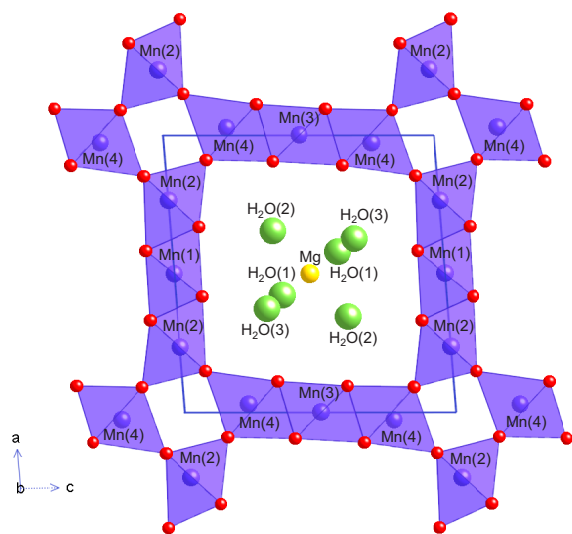

FIGURE 1. Polyhedral representation of the todorokite structure, viewed along *b*.

intensity synchrotron source offers improved counting statistics and dynamic range relative to conventional sealed-tube sources. Our synchrotron data also were collected using a capillary sample and imaging plate, with integration of full ring patterns, thereby eliminating preferred orientation effects. Additionally, we used real-time, temperature-resolved synchrotron X-ray diffraction data in conjunction with Rietveld refinements to investigate the behavior of the todorokite structure as it is heated from room temperature to 820 K. In this temperature range, todorokite dehydrates and transforms to hausmannite.

EXPERIMENTAL METHODS

Data collection

Diffraction data were collected using todorokite (Harvard University no. 126232) from the N'Chwaning Mine, North Cape Province, South Africa. This is the same sample that was used by Post and Bish (1988), who reported the following chemical formula for the mineral: $(Na_{0.40}, Ca_{0.14}, K_{0.01})(Mn^{4+}_{5.61}, Mg_{0.43})O_{12}\cdot$ $4.59H_2O$. The sample shows a fibrous habit and is, as far as we know, the most highly crystalline todorokite known (based on Bragg peak widths and selected area electron diffraction patterns), natural or synthetic. The sample was ground in an agate mortar to particle sizes below 400 mesh and loaded into 0.5 mm quartz-glass capillaries.

The X-ray diffraction data were collected at beam line X7B of the National Synchrotron Light Source (NSLS), Brookhaven National Laboratory (BNL). For the low-temperature experiment, the sample was cooled to 100 ± 5 K with an Oxford Cryosystems temperature controller using boiling liquid nitrogen. For the two high-temperature runs, the samples were heated from 298 K (RT) to 630 K and 820 K, at 3.2 and 2.9 K/min, respectively, using a Blake Instruments furnace with a Pt-13%Rh coiled wire yoke encased in ZrO_2 cement (Brown et al. 1973). The temperature was varied with an Omega controller

and monitored with a Chromel-Alumel thermocouple located ~2 mm from the specimen. The actual sample temperature was determined for the range 298 K to 1273 K by a variety of melting transitions and by the placement of an additional thermocouple in the sample position. The highly linear relationship between the observed and actual temperatures ($r^2 = 0.983$) allowed us to calculate a calibration curve with an estimated error of ±5 K for a given temperature. The X-ray wavelengths used were 0.9492 Å for the 100 K experiment and the heating run from 298 to 820 K, and 0.9370 Å for the data set from 298 to 630 K.

Intensities for the 100 K run were collected using a 120 s exposure with a 20 × 40 cm Fuji imaging plate mounted perpendicular to the incoming beam at a distance of 217.2 mm. The exposed plate was scanned with a Fuji BAS2000 reader, which yielded a nominal pixel size of 0.1×0.1 mm^2 (2048 × 4096 pixels) and a dynamic range of 10^4. Additional details for this procedure are provided by Norby (1997). The two sets of temperature-resolved data were collected using different experimental setups. The diffraction intensities for the 298 to 820 K experiment were measured using the Fuji imaging plate described above, but the plate was slowly translated past a vertical slit as the sample was heated. The resulting image provided a continuous, real-time record of X-ray diffraction intensities vs. temperature. Following the procedure described by Norby (1997), slices of intensity representing a specified temperature range, encompassing about 20 K each, were extracted from the imaging plate and used for the Rietveld refinement.

The second set of temperature resolved data, 298 to 630 K, was collected as a series of 120 s exposures with a MAR345 full imaging plate detector. The temperature was increased continuously and measurements were obtained every ~11 K; due to down time for repositioning of the sample and reading the imaging plate, each exposure represents a temperature range of ~5 K. During each exposure the sample was rotated through a 90° angle. Any preferred orientation of the powder should have been eliminated through a combination of the specimen rotation, use of a capillary sample holder, and full intensity integration of the diffraction rings, as obtained using the program Fit2D (Hammersley et al. 1996) with a polarization factor of 0.93.

Structure refinements

All refinements were performed with the General Structure Analysis System (GSAS) program of Larson and Von Dreele (2001). The starting parameters for the 100 and 298 K refinements were taken from Post and Bish (1988), but without the tunnel species. The refinement parameters included the scale factor and 30 to 36 background terms in a linear interpolation function. Peak profiles were modeled with a pseudovoigt profile function as parameterized by Thompson et al. (1987) with asymmetry corrections from Finger et al. (1994) and microstrain anisotropic broadening terms from Stephens (1999). After convergence of these parameters, the unit-cell dimensions were refined. At this point, a difference Fourier map was calculated to locate concentrations of electron density corresponding to tunnel cation/water sites. After adding these sites to the refinement, atomic positions, occupancy factors for the tunnel sites,

and isotropic atomic displacement factors were varied.

During refinement of the atom positions, soft constraints were applied to the Mn-O distances (constrained to 1.90 Å, with a standard deviation of 0.05 Å), and the weighting factor was gradually reduced in successive cycles. We found that even at the end of the refinement it was necessary to retain weak constraints (GSAS weighting factors of 1–3) on the Mn1-O and Mn3-O bonds. Without the constraints these distances refined to unrealistically short values of 1.81–1.83 Å.

The final refinement parameters for the 100 K and RT data sets are listed in Table 1. The atomic positions refined for the 100 K and RT data sets were not significantly different, so only the RT results are included in Table 2, and corresponding bond distances are reported in Table 3. The final observed, calculated, and difference powder diffraction patterns resulting from the Rietveld refinement using the 298 K data are plotted in Figure 2. Rietveld refinements were also performed for a series of XRD patterns from RT to near the todorokite-hausmannite transition temperature. These refinements did not yield significantly different framework atom positions, but revealed changes with temperature in the unit-cell parameters and tunnel sites (see below).

For the 100 K and RT data, we also performed a LeBail fit

to observed intensities, refining background, zero-shift, peak-shape parameters, and unit-cell parameters. We then performed a Rietveld refinement, using only the framework Mn and O atoms, and varying only the scale factor and background parameters. This procedure was followed in order to reduce correlations among the atom and overall profile parameters and to provide more detailed and unbiased difference Fourier maps for investigating the todorokite tunnel regions.

Estimation of errors

For our Rietveld analyses using synchrotron X-ray diffraction data collected with the Fuji imaging plate, the final χ^2 values typically fell below 1.00. The reduced χ^2 is calculated by GSAS as $\chi^2 = M/(N_{obs} - N_{var})$, where N_{obs} is the number of observed intensities and N_{var} is the number of refined variables. M is the function minimized during the refinement and is defined as $M = \Sigma w(I_o - I_c)^2$, where I_o and I_c are the observed and calculated intensities at a given value of 2θ and the weighting factor w is equal to the inverse of the square of the estimated standard deviation [i.e., $w = 1/(e.s.d.)^2$] (Larson and Von Dreele 2001). In our data sets, the e.s.d. for a given 2θ was arbitrarily calculated as the square root of the intensity. Because an amorphous component contributed very high background intensi-

TABLE 1. Final Rietveld refinement parameters for todorokite

	100 K	298 K
Space group	*P2/m*	*P2/m*
Unit cell		
a (Å)	9.760(1)	9.769(1)
b (Å)	2.8492(2)	2.8512(1)
c (Å)	9.549(1)	9.560(1)
β (°)	94.52(1)	94.47(1)
V (Å³)	264.71(5)	265.45(5)
Refinement		
No. of data points	1924	1924
No. of reflections	380	358
Diffraction range (2θ)	4.2–56.6°	4.2–56.6°
No. of variables	70	70
R (F²)	0.054	0.051
R_{wp}	0.030	0.035
χ^2	0.473	0.554

TABLE 2. Atomic coordinates and isotropic displacement factors for todorokite at 298 K

Atom	x	y	z	Site occupancy factor*	U_{iso} (Å²)†
Mn1	0.5	0.5	0	1.0	0.028(1)
Mn2	0.7638(5)	0	0.0002(6)	1.0	0.028(1)
Mn3	0	0	0.5	1.0	0.028(1)
Mn4	0.9725(6)	0.5	0.7650(6)	1.0	0.028(1)
O1	0.148(2)	0.5	0.084(2)	1.0	0.048(1)
O2	0.418(2)	0	0.096(2)	1.0	0.048(1)
O3	0.669(1)	0.5	0.102(2)	1.0	0.048(1)
O4	0.910(2)	0	0.150(2)	1.0	0.048(1)
O5	0.905(2)	0.5	0.395(1)	1.0	0.048(1)
O6	0.890(2)	0	0.650(1)	1.0	0.048(1)
$H_2O(1)$	0.421(3)	0	0.391(2)	0.84(4)	0.048
$H_2O(2)$	0.655(2)	0.5	0.373(2)	1.18(2)	0.048
$H_2O(3)$	0.626(4)	0.5	0.672(5)	0.61(4)	0.048
Mg	0.5	0.5	0.5	0.47(5)	0.048

* H_2O sites were refined as O, but might also include some Na and/or Ca.
† Isotropic displacement factors for like atoms were constrained to be equal, and for the H_2O and Mg sites were fixed to be equal to those for the O atoms.
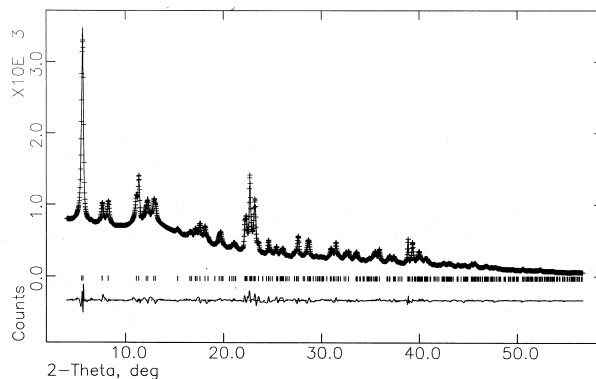

FIGURE 2. Final observed (crosses), calculated (solid line), and difference (lower) powder diffraction patterns for the Rietveld refinement using the 298 K todorokite data.

TABLE 3. Selected bond distances (Å) for todorokite at 298 K

Mn1-O2	1.90(1) ×4	Mn3-O5	1.94(1) ×4
Mn1-O3	1.86(1) ×2	Mn3-O6	1.86(1) ×2
<Mn1-O>	1.89	<Mn3-O>	1.91
Mn2-O1	1.88(1) ×2	Mn4-O1	1.93(1)
Mn2-O2	1.94(2)	Mn4-O4	1.97(1) ×2
Mn2-O3	1.99(1) ×2	Mn4-O5	2.02(1)
Mn2-O4	1.94(1)	Mn4-O6	1.94(1) ×2
<Mn2-O>	1.94	<Mn4-O>	1.96
$H_2O(1)$-O2	2.82(2)	$H_2O(3)$-O1	3.08(4)
$H_2O(1)$-O6	3.04(3)	$H_2O(3)$-O2	2.70(4) ×2
$H_2O(1)$-$H_2O(1)$	2.49(5)	$H_2O(3)$-O6	2.97(3) ×2
$H_2O(1)$-$H_2O(2)$	2.71(3)		
$H_2O(2)$-O3	2.61(2)	Mg-$H_2O(1)$	1.89(2) ×4
$H_2O(2)$-O5	2.43(2)	Mg-$H_2O(2)$	2.01(2) ×2
$H_2O(2)$-$H_2O(3)$	2.89(5)		
$H_2O(2)$-$H_2O(3)$	2.75(4)		

ties to our patterns, the calculated e.s.d.s for our patterns were unreasonably large. Consequently, the weighting factors w were unreasonably low, generating values for χ^2 that consistently fell below unity.

Inspection of the variation in the estimated standard deviation as a function of the scattering angle revealed no systematic dependence on 2θ. Consequently, the minimization calculations performed by GSAS were not biased by the unrealistic e.s.d. As a result, the final χ^2 values calculated during our analyses of the synchrotron X-ray diffraction data are meaningful as relative measures of the goodness of fit, albeit not as absolute measures. However, the reasonable bond distances and the low values for R_{wp} and R_{Bragg} provided independent measures of the accuracy of the final refined structure. As is often the case, the standard deviations calculated by GSAS for the lattice parameters are lower than the true errors (Post and Bish 1989). We present the errors calculated by GSAS in the tables and figures of this paper with the understanding that the actual errors may be more than an order of magnitude higher than the calculated deviations.

DISCUSSION

Octahedral framework

The 100 K and room temperature refinement results agree reasonably well with the todorokite structure reported by Post and Bish (1988), but provide improved precision for the bond distances in the octahedral framework. The Mn-O distances in Table 3 range from 1.86 to 2.02 Å, which fall within the range of Mn-O distances (1.86–2.12 Å) reported for the similar structures of hollandite and romanechite (Post et al. 1982; Turner and Post 1988). However, as discussed above, without soft constraints the refined Mn1-O3 and Mn3-O6 distances were unrealistic at 1.81 and 1.83 Å, respectively. Therefore, even though the estimated standard deviations determined by the Rietveld refinement are about 0.01 Å, the difference in bond lengths between constrained and unconstrained refinements suggests that the actual errors are probably two or three times that value.

Even when allowances are made for the true estimated errors in the reported Mn-O distances, the mean Mn2-O and Mn4-O distances (1.94 and 1.96 Å, respectively) are significantly longer than the mean Mn1-O and Mn3-O distances (1.89 and 1.91, respectively). The mean Mn-O distances for the Mn1 and Mn3 octahedra compare well with the Mn⁴⁺-O value of 1.89 Å measured for pyrolusite (Bauer 1976). Post and Bish (1988) suggested that the larger, lower valence cations, such as Mn³⁺ and Mg²⁺, preferentially occupy the Mn2 and Mn4 octahedra. This assignment is consistent with results from single-crystal diffraction studies of romanechite and woodruffite that show Mn³⁺ordering into the octahedral sites at the edges of the triple and quadruple chains, respectively (Turner and Post 1988; Post et al. 1999). As a pure MnO_2 framework is charge neutral, the lower valence octahedral cations are necessary to offset the charges of the cations in the tunnels.

Post and Bish (1988) speculated on the basis of cation-exchange studies and crystal chemical arguments that the Mg cations in todorokite are most likely located in framework octahedral sites, presumably Mn2 and Mn4. Recently, however,

Gutzmer and Beukes (2000) argued that their chemical analyses of todorokite samples from the same locality in the present study are consistent with Mg cations residing in the tunnels. Additionally, an X-ray spectroscopic study of Mn-oxide minerals by McKeown and Post (2001) showed that the average Mn valence for the same todorokite sample used here was approximately +3.7 to +3.8, thus supporting the conclusion that the low-valence octahedral cations that offset the intratunnel charge are Mn³⁺ and not Mg²⁺. If all of the lower valence cations in the octahedral framework are Mn³⁺, and they occur in the Mn2 and Mn4 sites, then approximately 40% of those sites must contain Mn³⁺ in order to offset the charges on the tunnel cations. The resulting mean Mn valence is 3.73, in good agreement with the XAS values reported by McKeown and Post (2001). Using the bond lengths of Shannon (1976) for Mn⁴⁺-O and Mn³⁺-O of 1.89 and 2.005 Å, respectively, we can calculate an expected mean Mn-O distance for Mn2 and Mn4 of 1.94 Å, which compares well with the observed values of 1.94 and 1.96 Å. The fact that the longest octahedral Mn-O distance for Mn4 is an axial bond is consistent with the Jahn-Teller distortion associated with Mn³⁺. If one assumes that all of the Mg is sited in the tunnels, the chemical formula for the todorokite sample used in this study is recalculated as:

$Mg_{0.45}Na_{0.42}Ca_{0.15}K_{0.01}(Mn^{4+}_{4.38}, Mn^{3+}_{1.62})O_{12} \cdot 4.0H_2O$.

Other low-valence cations sometimes found in natural or synthetic todorokite samples, e.g., Cu^{2+}, Ni^{2+}, and Co^{2+}, also likely occupy the larger Mn2 and Mn4 sites.

Tunnel water molecules and cations

The difference Fourier maps calculated for the 100 K refinement, using only the Mn-O framework, reveal at least four unique sets of electron density peaks in the todorokite tunnel regions, all located at $y = 0$ and $y = 1/2$ (Fig. 3). The difference Fourier maps calculated for the RT refinement were essentially identical to those at 100 K. The most prominent electron density peaks in Figure 3 at $y = 0$ and $y = 1/2$ correspond to the $H_2O(1)$ and $H_2O(2)$ sites, respectively, of Post and Bish (1988). The occupancy factors for both sites refined to values between 0.8 and 1.2 O atoms, consistent with approximately fully occupied water sites. Structure energy calculations performed by Post and Bish (1988) supported the assignment of water molecules to these sites, with $H_2O(1)$ being the most energetically favorable position. The difference map for $y = 1/2$ shows two additional electron density peaks; the one labeled $H_2O(3)$ in Figure 3 has a refined occupancy of about 0.6 O atoms, and another in the center of the tunnels, at (0.5,0.5,0.5), has an occupancy of 0.47(5) O atoms.

According to the revised chemical formula given above, the todorokite sample used in this study has a total of 1.03 cations and 4.0 water molecules per unit cell in the tunnels. Unfortunately, the similarity in X-ray scattering potential for Mg, O, and Na makes the assignment of specific tunnel species to particular sites problematic. Furthermore, the electron density maps suggest that the tunnel sites show positional disorder, both within and perpendicular to the mirror planes. Consequently, the refinements yield only average positions, and therefore, average bond lengths, that might deviate significantly from actual atomic distances. The positional disorder reflects the fact
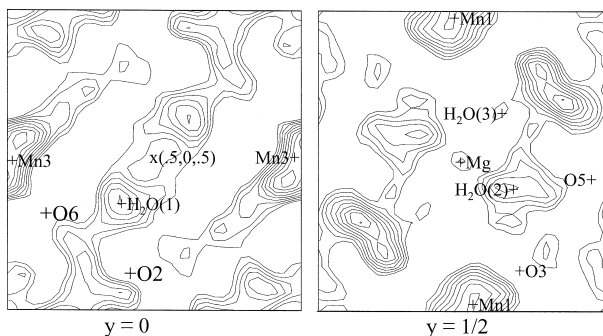
FIGURE 3. Difference Fourier maps calculated for the 100 K data using only the todorokite octahedral framework as the model structure, at (**a**) $y = 0$, and (**b**) $y = 1/2$. The contour interval is 0.15 e$^-$/Å^3. The negative electron density contours were omitted for clarity.

that several types of tunnel cations exhibit occupancies less than one. Consequently, the kinds of species within the tunnels and their spatial distribution may be fairly heterogeneous at the unit-cell scale. The cation and H_2O molecule positions most likely are also affected by the local arrangements of Mn^{3+} framework cations (Post and Burnham 1986).

The $H_2O(1)$ and $H_2O(2)$ sites, if fully occupied, can account for the four H_2O molecules per unit cell. It is also possible, however, that some, or all, of the Ca and Na cations might be disordered over these same sites. The $H_2O(2)$ distances to the nearest framework O atoms, for example, are 2.45 and 2.50 Å, which are short for O-O distances but are reasonable Na,Ca-O bond lengths. Also, the occupancy factor for this site is slightly (and perhaps not significantly) larger than 1.0, possibly due to a heavier atom such as Ca. The $H_2O(3)$ position is only partially filled and might be similarly disordered. The very short distance (1.60 Å) between $H_2O(1)$ and $H_2O(3)$ indicates that both sites cannot be simultaneously occupied in any given unit cell.

The structure-energy calculations performed by Post and Bish (1988) revealed that a cation likely resides at the centers of the tunnels at (0.5 0.5 0.5). In the present study, we refined an occupancy equivalent to about one-half of an O (or Mg or Na) atom at this position. This result agrees within error with the measured concentration of Mg in the structure. This site is surrounded by six tunnel H_2O molecules at the corners of an octahedron at distances ranging from 1.89 to 2.04 Å, which are reasonable Mg-O bond lengths. The relatively short bond lengths to the nearest H_2O positions argue that the larger Ca and Na cations must reside elsewhere, either at the H_2O sites, as mentioned above, or at other partially occupied sites that are not revealed in the electron density maps. The electron scattering represented by the sum of the refined occupancy factors for those intratunnel sites identified in our study closely matches the total value determined by chemical analyses, suggesting that all of the significant tunnel sites were identified.

Heating experiments

Our synchrotron X-ray diffraction data showed that todorokite, in vacuum, starts to transform to hausmannite in the temperature range 590 to 620 K (Fig. 4). Rietveld refine-

ments revealed a gradual thermal expansion of the todorokite structure to ~450 K (Fig. 5). At higher temperatures, the unit-cell volume gradually decreased, primarily as a result of a decrease in c, and the decline in β with increasing temperature was accelerated. The axial expansions of a and b, on the other hand, did not deviate from linearity until ~525 K, at which point a began a precipitous decline that continued to the transformation temperature, and b decreased more gradually.

In addition to the changes in the unit-cell parameters described above, at ~450 K the overall intensity of the todorokite diffraction pattern (as represented by the refined scale factor) started to decrease, suggesting that some todorokite was decomposing. The decline in overall peak intensities (and scale factors) with increasing temperature continued to the transformation temperature. The change was especially obvious for the unresolved (001) and (100) reflections (Fig. 4). This observation is consistent with thermogravimetric analyses (TGA) of todorokite samples by Bish and Post (1989), who showed that weight losses in N_2 and O_2 atmospheres deviated from each other at about 475 K, with weight losses occurring at higher temperatures in O_2. They interpreted this discrepant behavior as evidence that framework O is released as Mn is reduced, and they argued that the divergence of the weight loss curves marked the beginning of the breakdown of the todorokite structure in an oxygen-free atmosphere. Shen et al. (1993) observed loss of O_2 from a synthetic Mg-rich todorokite beginning at approximately 523 K. The higher O_2-loss temperature for the synthetic sample in comparison with the results of Bish and Post (1989) might be due to differences in composition and/or heating conditions.

Mass spectrometer analyses of effluents during our synchrotron heating experiment showed that water loss from the todorokite sample began at ~450 K and attained a maximum at ~590 K (Fig. 6). Bish and Post (1989) measured water loss vs. temperature using the same todorokite sample used in this study and observed that the major water release started below 473 K and was nearly complete by about 573 K.

It might seem logical to assume that water loss from the tunnels of todorokite leads to collapse of the framework. How-
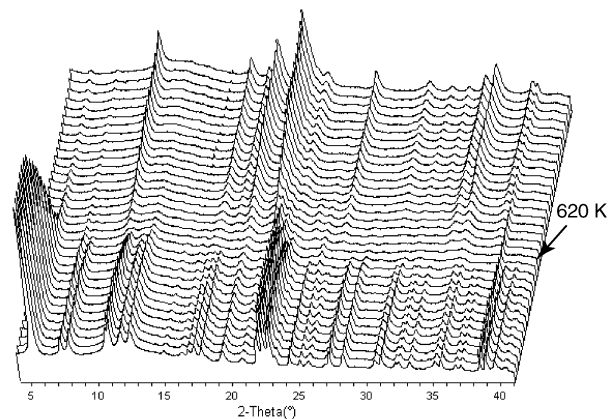

FIGURE 4. Synchrotron XRD patterns for todorokite vs. temperature, 298 to 820 K.

ever, our observation that the loss of structural water and the breakdown of the octahedral framework begin at approximately the same temperature strongly argues that the reverse is actually true. The reduction of Mn and the loss of O trigger a breakdown of the octahedral framework that in turn drives the release of the tunnel water molecules. This conclusion is supported by the fact that the refined occupancy factors for the tunnel H_2O sites in the temperature range 475 and 600 K are not significantly lower than their RT values. Apparently, as todorokite
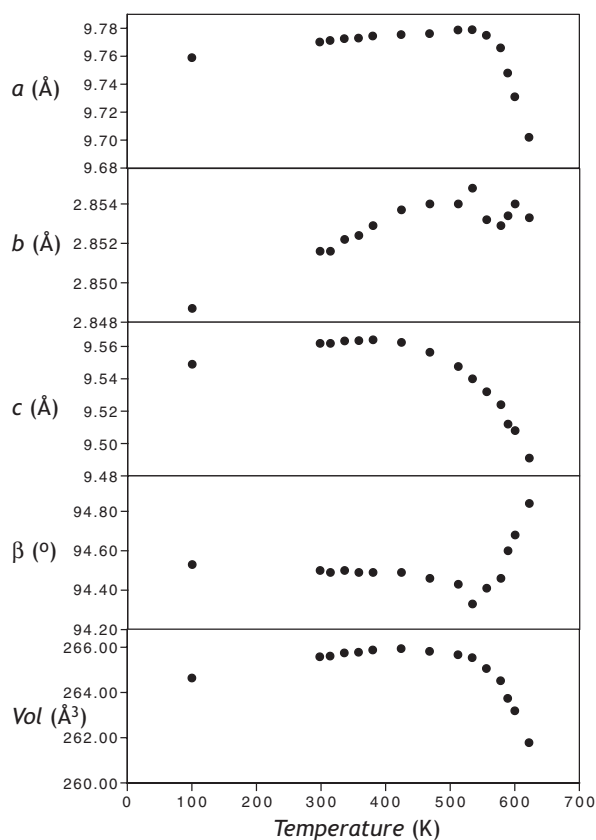

FIGURE 5. Plots showing changes in todorokite unit-cell parameters during heating.

FIGURE 6. Water loss from todorokite, as measured by mass spectrometer vs. temperature in vacuum.

breaks down at high temperature, water is released, but the portion of the sample still contributing to the X-ray diffraction pattern retains its full complement of water.

Thermal stability of todorokite

Most published studies of todorokite thermal behavior have employed synthetic todorokite-like phases, and in general, are consistent with the work described here. Previous TGA experiments (e.g., Vileno et al. 1999; Shen et al. 1993; Duncan et al. 1998) generally reveal a loss of water between 473 and 650 K. Variations in the reported temperature range can be explained by differences in sample composition and crystallinity, and data collection conditions. One point of some disagreement, however, is the temperature to which the todorokite structure remains stable. On the basis of the continued presence of the (100,001) diffraction peak, Bish and Post (1989) conclude that todorokite is stable to at least 773 K. Shen et al. (1993) also suggest that synthetic Mg-todorokite is stable to that temperature. On the other hand, Ching et al. (1999) note that while the XRD pattern for synthetic Mg-todorokite appeared unchanged after heating to 573 K, the (100,001) peak was almost undetectable by 673 K and had disappeared by 773 K. Also, Shen et al. (1996) conclude that heating synthetic Cu-todorokite to 621 K destroyed the tunnels.

Our synchrotron X-ray diffraction data clearly showed that the todorokite structure had fully decomposed by ~620 K. Since our experiments were carried out under vacuum, the breakdown temperature might have shifted to a lower value than that in air. A remnant of the todorokite (100,001) peak persisted above 620 K, but it was significantly broadened and at less than 5% of its RT intensity. Virtually all of the remaining peaks, however, had disappeared by 620 K, at which point the first hausmannite diffraction peaks became visible.

It is interesting to note that the remnant (001,100) peak never completely disappeared, even at the maximum temperature of 820 K for our first experimental run. This persistence strongly implies that the peak at high temperatures arose from a phase that formed secondarily with hausmannite above 620 K. One possible candidate would be a compound that accommodated the Na and Ca cations originally present in the parent todorokite sample, as these large cations could not be easily accommodated by the hausmannite structure. A Rietveld refinement of the hausmannite formed during the heating experiments revealed several extra low-intensity diffraction peaks. We were not able to match these extra peaks to known Na/Ca Mn-oxides, but several of the lines, including the one at ~9.6 Å, are close to those measured for $K_2Mn_4O_9$ by Endo et al. (1974), suggesting a Na/Ca analogue of that phase.

The steady increase in the intensity of the hausmannite diffraction peaks as the sample is heated above ~620 K mirrors the gradual decomposition of the todorokite structure. The relatively slow formation of hausmannite is consistent with TGA results showing a continued O_2 weight loss up to about 860 K in N_2 (and about 950 K in O_2) (Bish and Post 1989). These authors found evidence for a marked increase in the release of O_2 between 810 and 860 K (in an N_2 atmosphere), and this O_2 loss probably corresponds to an interval of major hausmannite formation.
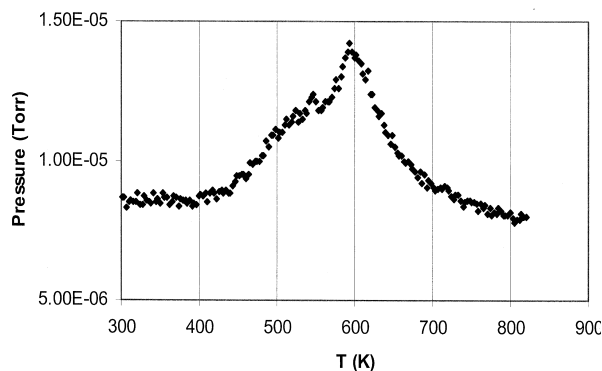
Between approximately 625 and 745 K, a diffraction line builds at 2.18 Å and disappears (Fig. 4). This line does not belong to hausmannite or todorokite, or any other known Na or Ca manganese oxide phases. Possibly it arises from some intermediate, disordered hausmannite structure.

Structural changes during the todorokite to hausmannite transformation

X-ray diffraction, mass spectrometer, and TGA (Bish and Post 1989) data show that the transformation of the todorokite structure to hausmannite occurs gradually between ~450 and ~620 K. Two factors may contribute to the protracted quality of the breakdown reaction for todorokite. First, todorokite samples typically contain significant structural disorder, such as intergrowths of Mn octahedral chains with different widths, and the more heavily disordered regions might be less thermally stable and transform at lower temperatures. Second, as was described above, the tunnel contents for different unit cells can vary, and some compositions might be more thermally stable than others.

The onset of todorokite decomposition (~450 K) coincides with the point at which the unit-cell volume and the value of c start to decrease (Fig. 5). Since the structural breakdown is initiated by reduction of the Mn valence and O loss, perhaps some of the Mn^{3+} in the todorokite that persists is reduced to Mn^{2+}. The consequent easing of Jahn-Teller octahedral distortions, which are most pronounced in the ac plane, could explain the decrease in c and the change in the rate at which β decreases at 450 K.

The absolute changes in the unit-cell parameters of todorokite are relatively small, perhaps surprisingly so for a structure that contains such large tunnels. The total changes in the a and c parameters between 100 and 620 K, for example, are less than 0.08 Å each, or about 0.8%, and b changes by only 0.2%. In the same range, β varies by less than 0.5°, and the unit-cell volume by approximately 1.5% (Fig. 5). Up to the temperature at which the reduction of framework Mn triggers its decomposition, the todorokite structure is impressively rigid.

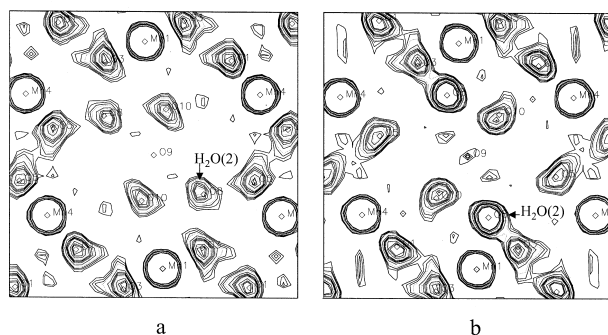Difference Fourier maps for the tunnel region (Fig. 7) show

FIGURE 7. Observed electron density maps showing todorokite tunnel region at $y = {}^1/_2$ for (**a**) ~600 K and (**b**) ~620 K. The contour interval is 0.5 e⁻/Å³. The negative electron density contours were omitted for clarity.

that beginning at ~575 K the $H_2O(2)$ site shifts closer to O3 in the octahedral framework (Fig. 1), and the refined occupancy factor for $H_2O(2)$ increases to over 2.5 O atom equivalents. Because these results were based on refinements at temperatures at which most of the todorokite had decomposed, it is possible that the calculated changes in $H_2O(2)$ were an artifact. As the agreement factors were quite good and the structural parameters seemed well behaved, we conclude that the changes in $H_2O(2)$ are real. Consequently, it appears that the O atom at the $H_2O(2)$ site is being replaced with an atom having more than twice the X-ray scattering power of O near the temperature at which hausmannite starts to form.

It seems likely that as the todorokite framework breaks down, some of the Mn atoms move into the tunnels. This explanation is supported by the fact that the refined occupancy for the new $H_2O(2)$ site is approximately that of one Mn atom (i.e., 2.5 O atoms). In addition, the distance from the new tunnel site to the nearest framework O atom is 2.0 Å, which is a reasonable Mn-O bond length and an unreasonable O-O distance. The proposed tunnel Mn site is an unrealistic 2.2 Å from the framework Mn1 atom, but this problem is resolved if the migration of Mn atoms to the tunnel sites is accompanied by the removal of alternate Mn1 atoms, as posited in the todorokite-hausmannite transformation model given below.

A mechanism for the todorokite to hausmannite transformation

In the range of approximately 590 to 620 K, the todorokite diffraction pattern essentially disappears and hausmannite diffraction peaks appear (Fig. 4). The hausmannite peaks sharpen and increase in intensity as the sample is heated to 820 K, the maximum temperature for our heating experiment. The relatively narrow temperature range encompassing the transformation from todorokite to hausmannite and the coincidence of several of the todorokite and hausmannite diffraction lines seem to argue for a mechanism that builds the hausmannite structure from that of todorokite, as opposed to a model in which hausmannite rises from the ashes of a completely destroyed todorokite framework.

Figure 8 depicts one possible mechanism for forming the inverse spinel structure of hausmannite from todorokite. As is consistent with the results described above, the first step entails the migration of half of the Mn1 cations from the central octahedra in the layered triple chains to nearby tunnel positions, where the cations adopt tetrahedral coordination in the final hausmannite structure (Fig. 8a). In the next stage of transformation, Mn^{4+} in the todorokite framework is reduced to Mn^{2+} and Mn^{3+}, and one-third of the O atoms exit the structure (Fig. 8b). Within one unit cell of todorokite, this reaction is represented as follows:

$$Mn_{12}^{4+}O_{24} \quad \rightarrow \quad (Mn^{3+}, Mn^{2+})_8 Mn_4^{3+}O_{16} + 4O_2.$$

idealized todorokite   hausmannite
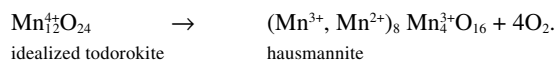
In our model, we preserve the nearly closest packed oxygen sheets along (100) that comprise one edge of the tunnels outlined by the triple chains. This assumption is based on the integrity of closest packed O sheets in other structures that
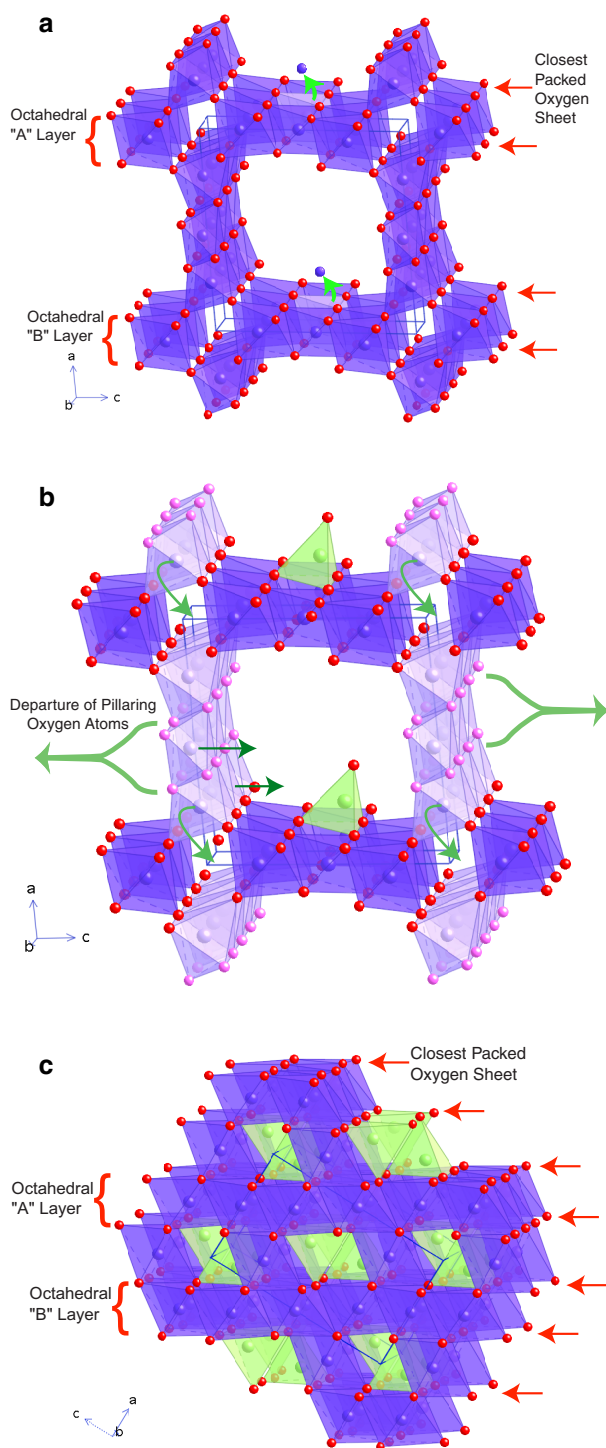
FIGURE 8. A possible scheme for the transformation of todorokite to hausmannite: (**a**) todorokite octahedral framework, projected down *b*; the highlighted O atoms are lost as the Mn atoms are reduced from +4 and +3 to +2 and +3, (**b**) The Mn from the disrupted octahedra move into the large and small tunnels, and (**c**) the remnants of the todorokite structure collapse together and new Mn-O bonds form to build the hausmannite structure.

undergo phase transitions, such as the olivine-wadsleyite transition (Burnley and Green 1989), and it is supported by the persistence through the transition of the (200) reflection of todorokite as the (101) reflection in hausmannite, since the closest packed O atoms in hausmannite are parallel to (101). In this conception, the triple chains parallel to (001) (oriented vertically in Fig. 8a) can be considered pillars that support the closest packed layers of triple chains parallel to (100) (oriented horizontally in Fig. 8a).

Thus, in this second stage of the transformation, the O atoms that comprise the layered triple chains retain their structural integrity, but the O atoms that frame the central octahedra in the pillaring triple chains escape the structure as free O atoms (Fig. 8b). There are 8 such O atoms per unit cell, and they are released as O_2 molecules. As these O atoms volatilize, the Mn1 cations within the disrupted octahedra migrate to tunnel sites.

The disruption of the central octahedra along the pillaring triple chains leads to a structural collapse of the stacking modules parallel to (001). As this collapse occurs, the residual Mn2 cations in the pillaring octahedra diffuse from their sites. Some migrate to the octahedrally coordinated sites in the small tunnels parallel to *b* at the origins of the todorokite cell, and some move to tunnel sites where they assume octahedral coordination in the hausmannite structure (Fig. 8c).

The process diagrammed in Figure 8 results in a reduction of volume of ~45% when normalized to 1 Mn cation, which agrees well with the observed value of about 41%. Clearly, this is not the only model for the todorokite-to-hausmannite transformation, but it is structurally reasonable and most consistent with our observations.

A Rietveld refinement for the cooled hausmannite yielded an occupancy factor for the tetrahedral Mn site of 0.90(2), which agrees well with the predicted value of 0.94, assuming all of the Mg in todorokite (0.45 Mg per 6 Mn atoms) ordered into that site. Considering the strong preference for Mn^{3+} to form Jahn-Teller distorted octahedra, it is reasonable that the Mg cations would selectively occupy the tetrahedral Mn^{2+} site, as it does in many spinel structures.

REFERENCES CITED

Bauer, W.H. (1976) Rutile-type compounds. V. Refinement of MnO_2 and MgF_2. Acta Crystallographica, B32, 2200–2204.
Bish, D.L. and Post, J.E. (1989) Thermal behavior of complex, tunnel-structure manganese oxides. American Mineralogist, 74, 177–186.
Brock, S.L., Duan, N., Tian, Z.R., Giraldo, O., Zhou, H., and Suib, S.L. (1998) A review of porous manganese oxide materials. Chemistry of Materials, 10, 2619–2628.
Brown, G.E., Sueno, S., and Prewitt, C.T. (1973) A new single-crystal heater for the precession camera and four-circle diffractometer. American Mineralogist, 58, 698–704.
Burnley, P.C. and Green, H.W. (1989) Stress dependence of the mechanism of the olivine-spinel transformation. Nature, 338, 753–756.
Ching, S., Katarzyna, S., Krukowska, S., and Suib, S.L. (1999) A new synthetic route to todorokite-type manganese oxides. Inorganica Chimica Acta, 294, 123–132.
Duncan, M.J., Leroux, F., Corbett, J.M., and Nazar, L.F. (1998) Todorokites as a Li

insertion cathode. Journal of the Electrochemical Society, 145, 3746–3757.

Dyer, A., Pillinger, M., Newton, J., Harjula, R., Möller, T., and Amin, S. (2000) Sorption behavior of radionuclides on crystalline synthetic tunnel manganese oxides. Chemistry of Materials, 12, 3798–3804.

Endo, T., Kume, S., Shimada, M., and Koizumi, M. (1974) Synthesis of potassium manganese oxides under hydrothermal conditions. Mineralogical Magazine, 39, 559–563.

Finger, L.W., Cox, D.E., and Jephcoat, A.P. (1994) A correction for powder diffraction peak asymmetry due to axial divergence. Journal of Applied Crystallography, 27, 892–900.

Golden, D.C., Chen, C.C., and Dixon, J.B. (1986) Synthesis of todorokite. Science, 231, 717–719.

Gutzmer, J. and Beukes, N.J. (2000) Asbestiform manjiroite and todorokite from the Kalahari manganese field, South Africa. South African Journal of Geology, 103, 163–174.

Hammersley, A.P., Svensson, S.O., Hanfland, M., Fitch, A.N., and Hausermann D. (1996) Two-dimensional detector software: From real detector to idealised image or two-theta scan. High Pressure Research, 14, 235–248.

Kanoh, H., Tang, W., Makita, Y., and Ooi, K. (1997) Electrochemical intercalation of alkali-metal ions into birnessite-type manganese oxide inaqueous solution. Langmuir, 13, 6845–6849.

Larson, A.C. and Von Dreele, R.B. (2001) GSAS-General Structure Analysis System. Los Alamos National Laboratory Report No. LAUR 86–748.

Luo, J., Zhang, Q., Huang, A., Giraldo, O., and Suib, S.L. (1999) Double-aging method for preparation of stabilized Na-buserite and transformation to todorokites incorporated with various metals. Inorganic Chemistry, 38, 6106–6113.

McKeown, D.A. and Post, J.E. (2001) Characterization of manganese oxide mineralogy in rock varnish and dendrites using X-ray absorption spectroscopy. American Mineralogist, 86, 701–713.

Nicolas-Tolentino, E., Tian, Z.R., Zhou, H., Xia, G., and Suib, S.L. (1999) Effects of Cu^{2+} ions on the structure and reactivity of todorokite- and cryptomelane-type manganese oxide octahedral molecular sieves. Chemistry of Materials, 11, 1733–1741.

Nitta, M. (1984) Characterization of manganese nodules as adsorbents and catalysts, a review. Applied Catalysis, 9, 151–176.

Norby, P. (1997) Synchrotron powder diffraction using imaging plates: Crystal structure determination and Rietveld refinement. Journal of Applied Crystallography, 30, 21–30.

Post, J.E. and Bish, D.L. (1988) Rietveld refinement of the todorokite structure American Mineralogist, 73, 861–869.

———(1989) Rietveld refinement of crystal structures using powder X-ray diffraction data. Reviews in Mineralogy, 20, 277–308.

Post, J.E and Burnham, C.W. (1986) Modeling tunnel-cation displacements in hollandites using structure-energy calculations. American Mineralogist, 71, 1178–1185.

Post, J.E., Von Dreele, R.B., and Buseck, P.R. (1982) Symmetry and cation displacements in hollandites: structure refinements of hollandite, cryptomelane, and priderite. Acta Crystallographica, B38, 1056–1065.

Post, J.E., Finger, L.W., and Heaney, P.J. (1999) Crystal structure of woodruffite: a Mn oxide with a 3×4 tunnel structure. Geological Society of America Abstracts, A356–A357.

Shannon, R.D. (1976) Revised effective ionic radii and systematic studies of interatomic distances in halides and chalcogenides. Acta Crystallographica, A32, 751–767.

Shen, Y.F., Zerger, R.P., DeGuzman, R.N., Suib, S.L., McCurdy, L., Potter, D.I., and O'Young, C.L. (1993) Manganese oxide octahedral molecular sieves: preparation, characterization, and applications. Science, 260, 511–515.

Shen, Y., Suib, S.L., and O'Young, C. (1996) Cu containing octahedral molecular sieves and octahedral layered materials. Journal of Catalysis, 161, 115–122.

Stephens, P.W. (1999) Phenomenological model of anisotropic peak broadening in powder diffraction. Journal of Applied Crystallography, 32, 281–289.

Thompson, P., Cox, D.E., and Hastings, J.B. (1987) Rietveld refinement of Debye-Scherrer synchrotron X-ray data from Al_2O_3. Journal of Applied Crystallography, 20, 79–83.

Turner, S. and Post, J.E. (1988) Refinement of the substructure and superstructure of romanechite. American Mineralogist. 73, 1155–1161.

Vileno, E., Zhou, H., Zhang, Q., Suib, S.L., Corbin, D.R., and Koch, T.A. (1999) Synthetic todorokite produced by microwave heating: an active oxidation catalyst. Journal of Catalysis, 187, 285–297.

Weisz, P. B. (1968) Deep sea manganese nodules as oxidative catalysts. Journal of Catalysis, 10, 407–412.